

# Entropy-regularized Maximum-Likelihood cluster mass reconstruction

Stella Seitz<sup>1,2</sup>, Peter Schneider<sup>2</sup> and Matthias Bartelmann<sup>2</sup>

<sup>1</sup> Universitätssternwarte München, Scheinerstr. 1, D-81679 München, Germany

<sup>2</sup> Max-Planck-Institut f. Astrophysik, Postfach 1523,  
D-85740 Garching, Germany

## Abstract

We present a new method for reconstructing two-dimensional mass maps of galaxy clusters from the image distortion of background galaxies. In contrast to most previous approaches, which directly convert locally averaged image ellipticities to mass maps (direct methods), our entropy-regularized maximum-likelihood method is an inverse approach. Albeit somewhat more expensive computationally, our method allows high spatial resolution in those parts of the cluster where the lensing signal is strong enough. Furthermore, it allows to straightforwardly incorporate additional constraints, such as magnification information or strong-lensing features. Using synthetic data, we compare our new approach to direct methods and find indeed a substantial improvement especially in the reconstruction of mass peaks. The main differences to previously published inverse methods are discussed.

## 1 Introduction

The reconstruction of projected cluster mass maps from the observable image distortion of faint background galaxies due to the tidal gravitational field is a new and powerful technique. Pioneered by Kaiser & Squires (1993), this method has since been modified and generalized to account for (a) strong tidal fields in cluster centers (Schneider & Seitz 1995; Seitz & Schneider 1995; Kaiser 1995); (b) finite and – in some cases, e.g. WFPC2 images – very small data fields (Schneider 1995; Kaiser et al. 1995; Bartelmann 1995; Seitz & Schneider 1996, 1998; Lombardi & Bertin 1998); and (c) the broad redshift distribution of background galaxies (Seitz & Schneider 1997). All of these are direct methods in the sense that a local estimate of the tidal field is derived from observed galaxy ellipticities, which is then inserted into an inversion equation to obtain an estimate of the surface mass density of the cluster.

Whereas these direct methods are computationally fast, can be treated as black-box routines, need only the observed ellipticities and a smoothing length  $\theta_0$  as input data, and yield fair estimates of the surface mass density, their application has several drawbacks:

- The data must be smoothed, and the smoothing scale is typically a free input parameter specified prior to the mass reconstruction. There are no objective criteria on how to set the smoothing scale, although some ad-hoc prescriptions for adapting it to the strength of the lensing signal have been given (Seitz et al. 1996). In general, smoothing leads to an underestimate of the surface mass density in cluster centers or sub-condensations.
- The quality of the reconstruction is hard to quantify.
- Constraints on the mass distribution from additional observables (such as multiple images or giant arcs) cannot simultaneously be included. In particular, magnification information contained in the number density of background sources (Broadhurst et al. 1995; Fort et al. 1997) or in the image sizes at fixed surface brightness (Bartelmann & Narayan 1995), cannot

be incorporated locally but only globally to break the mass-sheet degeneracy (Gorenstein et al. 1988; Schneider & Seitz 1995).

To overcome these drawbacks, a different class of methods should be used. Bartelmann et al. (1996, hereafter BNSS) developed a maximum-likelihood (ML) technique in which the values of the deflection potential at grid points are considered as free parameters. After averaging image ellipticities and sizes over grid cells, local estimates of shear and magnification are obtained. The deflection potential at the grid points is then determined such as to optimally reproduce the observed shear and magnification estimates. Magnification information can be included this way. The smoothing scale in this method is given by the size of the grid cells, and can be chosen such that the overall  $\chi^2$  of the fit is of order unity per degree of freedom.

Squires & Kaiser (1996; hereafter SK) suggested several inverse methods. Their *maximum probability method* parameterizes the mass distribution of the cluster by a set of Fourier modes. If the number of degrees of freedom (here the number of Fourier modes) is large, the mass model tends to over-fit the data. This has to be avoided by regularizing the model, for which purpose SK impose a condition on the power spectrum of the Fourier modes. SK's *maximum-likelihood method* specifies the surface mass density on a grid and uses the Tikhonov-Miller regularization (Press et al. 1992, Sect. 18.5). The smoothness of the mass reconstructions can be changed by varying the regularization parameter, which is chosen such as to give an overall  $\chi^2 \approx 1$  per degree of freedom.

Bridle et al. (1998) have recently proposed an entropy-regularized ML method in which the cluster mass map is parameterized by the surface mass density at grid points. This method allows to restrict the possible mass maps to such with non-negative surface mass density.

This paper describes another variant of the ML method (Seitz 1997, Ph.D. thesis). The major differences to the previously mentioned inverse methods are the following:

- The observational data (e.g. the image ellipticities) are not smoothed, but each individual ellipticity of a background galaxy is used in the likelihood function. Whereas this modification complicates the implementation of the method, it allows larger spatial resolution for a given number of grid points, which is useful since the latter determines the computing time.
- The number of grid points can be much larger than in BNSS, and the likelihood function is regularized. This produces mass reconstructions of variable smoothness: Mass maps are smooth where the data do not demand structure, but show sharp peaks where required by the data. The resulting spatially varying smoothing scale is a very desirable feature. Fourier methods, such as SK's maximum probability method, have a spatially constant smoothing scale which is determined by the highest-order Fourier components. They always need to compromise between providing sufficient resolution near mass peaks and avoiding over-fitting of the data in the outer parts of a cluster.
- Following BNSS, we use the deflection potential to describe a cluster. This is an essential difference to Bridle et al. (1998) who used the surface mass density at grid points. As we shall discuss below, working with the deflection potential has substantial fundamental and practical advantages.

We describe our method in Sect. 2, with details given in the Appendix. We then apply the method to synthetic data sets in Sects. 3 & 4 to demonstrate its accuracy. In particular, we compare the performance of our ML method to that of direct methods. The results are then discussed in Sect. 4, and conclusions are given in Sect. 5, where we also discuss further generalizations of the method for, e.g., including constraints from strong lensing features.

## 2 The entropy-regularized ML mass reconstruction

## 2.1 Basic lensing relations

For simplicity, we assume throughout the paper that all background galaxies are located at the same redshift. A generalization of our technique to a redshift distribution is given by Geiger & Schneider (1998). The dimensionless surface mass density  $\kappa(\vec{\theta})$  is related to the deflection potential  $\psi(\vec{\theta})$  through the Poisson equation,

$$\kappa(\vec{\theta}) = \frac{1}{2} (\psi_{,11} + \psi_{,22}) , \quad (1)$$

where indices  $i$  preceded by a comma denote partial derivatives with respect to  $\theta_i$ . The tidal gravitational field of the lens is described by the shear  $\gamma = \gamma_1 + i\gamma_2$  with the two components

$$\gamma_1 = \frac{1}{2} (\psi_{,11} - \psi_{,22}) , \quad \gamma_2 = \psi_{,12} . \quad (2)$$

Thus, the surface mass density and the shear, which determine the local properties of the lens mapping, can *locally* be obtained from the deflection potential  $\psi$ . In contrast, the relation between shear and surface mass density is highly non-local,

$$\gamma(\vec{\theta}) = \frac{1}{\pi} \int_{\mathbb{R}^2} d^2\theta' \mathcal{D}(\vec{\theta} - \vec{\theta}') \kappa(\vec{\theta}') , \quad (3)$$

with  $\mathcal{D}(\vec{\theta}) = -(\theta_1^2 - \theta_2^2 + 2i\theta_1\theta_2)|\vec{\theta}|^{-4}$ . In particular,  $\kappa$  needs to be given on the entire two-dimensional plane. Prescribing  $\kappa$  on a finite field does therefore not completely specify the shear inside the field, because the latter is also affected by the outside mass distribution. We return to this point further below. The local magnification is

$$\mu(\vec{\theta}) = \left\{ \left[ 1 - \kappa(\vec{\theta}) \right]^2 - \left| \gamma(\vec{\theta}) \right|^2 \right\}^{-1} . \quad (4)$$

The local lens equation relates the ellipticities of a source and its image. We use the complex ellipticity parameter  $\chi$  (see Blandford et al. 1991) to describe image shapes. It is generally defined in terms of the tensor  $Q_{ij}$  of second brightness moments of an image by  $\chi = (Q_{11} - Q_{22} + 2iQ_{12}) / (Q_{11} + Q_{22})$ .

## 2.2 The ML method

We refer the reader to Press et al. (1992, Chap. 18) for the basic ingredients of the ML method; see also Bridle et al. (1998). We do not repeat the basics here, but describe the application of the method to the cluster mass reconstruction. We start by considering image ellipticities only; magnification effects will be discussed later.

Let  $\chi_k$ ,  $1 \leq k \leq N_g$ , denote the complex ellipticities of  $N_g$  galaxy images in the data field  $\mathcal{U}$ , which we assume to be a rectangle of side lengths  $L_x$  and  $L_y$ . We cover the data field with an equidistant grid of  $N_x \times N_y$  points  $\vec{\theta}_{ij}$ , with  $\vec{\theta}_{11}$  in the lower left corner of the data field. The cluster is described by the deflection potential at the grid points,  $\psi_{ij}$ ,  $0 \leq i \leq N_x + 1$ ,  $0 \leq j \leq N_y + 1$ . As discussed in BNSS, the grid for  $\psi$  is larger than the data field by one column or row of grid points in all four directions to allow simple finite differencing of  $\psi$  on the whole field  $\mathcal{U}$ . Having found  $\kappa$  and  $\gamma$  on all grid points from  $\psi$  according to (1) and (2),  $\kappa$  and  $\gamma$  are bilinearly interpolated to all galaxy positions  $\vec{\theta}_k$ .

If the isotropic probability distribution  $p_s(\chi^s)$  of the intrinsic source ellipticities is given, the probability distribution  $p(\chi; \{\psi\})$  of the image ellipticities can be predicted. The likelihood function is then defined as

$$\mathcal{L}(\{\psi\}) := \prod_{k=1}^{N_g} p(\chi_k; \{\psi\}) . \quad (5)$$

$\mathcal{L}$ , or  $\ln \mathcal{L}$ , can be maximized with respect to the set  $\{\psi\}$  of values of the deflection potential at the grid points. Since the values of  $\kappa$  and  $\gamma$  are obtained from second derivatives of  $\psi$ , a constant and a term linear in  $\vec{\theta}$  added to  $\psi$  leave  $\mathcal{L}$  unchanged. In addition, the mass-sheet degeneracy renders  $\mathcal{L}$  invariant under the transformation

$$\psi(\vec{\theta}) \rightarrow \lambda \psi(\vec{\theta}) + \frac{(1-\lambda)}{2} |\vec{\theta}|^2, \quad (6)$$

where  $\lambda \neq 0$  is an arbitrary parameter (Schneider & Seitz 1995). Therefore, in maximizing  $\mathcal{L}$  with respect to  $\{\psi\}$ , the potential  $\psi$  can be held fixed at four grid points. Noting that the corners of the  $\psi$  grid are not used for the calculation of  $\kappa$  and  $\gamma$  on  $\mathcal{U}$  (see Appendix), we see that the maximization of  $\mathcal{L}$  has dimension  $N_{\text{dim}} = (N_x + 2)(N_y + 2) - 8$ .

### 2.3 Regularization

Provided  $N_{\text{dim}}$  is not much smaller than the number of galaxies (which we assume in the following), the maximization results in a cluster model which tries to follow closely the noise pattern of the data. Disregarding observational effects, the noise is due to the intrinsic ellipticity distribution of the sources. The reconstructed mass distribution will therefore have pronounced small-scale structure, fitting the observed image ellipticities as closely as possible, and having a  $\chi^2$  per degree of freedom much smaller than unity. In order to prevent such over-fitting of the data, we need to augment  $\mathcal{L}$  by a regularization term. Instead of maximizing  $\ln \mathcal{L}$ , we minimize

$$E(\{\psi\}) := -\frac{1}{N_g} \ln \mathcal{L}(\{\psi\}) + \eta \mathcal{R}(\{\psi\}), \quad (7)$$

where  $\mathcal{R}$  is a function of the potential that disfavors strong small-scale fluctuations. The parameter  $\eta$  determines how much weight should be attached to smoothness. One can vary  $\eta$  such that the resulting reconstruction has approximately the expected deviation from the data, viz.  $\chi^2 \approx 1$  per degree of freedom. Larger values of  $\eta$  yield mass distributions which are too smooth to fit the data, lower values of  $\eta$  cause over-fitting.

We experimented with quite a large number of regularization terms. For example, we chose  $\mathcal{R}$  as the sum of  $|\nabla \kappa|^2$  over all grid points. Mass reconstructions from synthetic data (see Sect. 3 below) then showed a strong tendency to decrease too slowly towards the outer parts of the cluster, for that regularization preferred  $\kappa$  to be as flat as possible. Regularizations including higher-order derivatives of  $\kappa$  (see Press et al. 1992, Sect. 18.5) led to similar artifacts. Thus, such local linear regularizations were dismissed as unsatisfactory.

Motivated by the success of the maximum-entropy (ME) image deconvolution (e.g. Narayan & Nityananda 1986; Lucy 1994), we consider instead ME regularizations of the form

$$\mathcal{R} = \sum_{i,j=1}^{N_x, N_y} \hat{\kappa}_{ij} \ln \left( \frac{\hat{\kappa}_{ij}}{b_{ij}} \right), \quad (8)$$

where

$$\hat{\kappa}_{ij} = \left[ \sum_{k,l=1}^{N_x, N_y} \kappa_{kl} \right]^{-1} \kappa_{ij} \quad (9)$$

is the normalized surface mass density at the grid points, and  $b_{ij}$  is a similarly normalized prior distribution (see Press et al. 1992, Sect. 18.7, for a detailed discussion of the ME method). We experimented with different choices for the prior. On the whole, a uniform prior,  $b_{ij} = \text{const.}$ , performed satisfactorily, but tended to smooth mass peaks more than desired. Following Lucy (1994), we therefore use a prior which is determined by the data itself. Deferring details to Sect. 3, we note here that one can use the mass distribution obtained from a direct (finite field) reconstruction method as an initial prior, then iteratively minimize  $E$ , and after several iterations use a smoothed version of the current mass distribution as a new prior. Lucy (1994) showed that

such a moving prior yields more accurate reconstructions than a constant prior. The regularization parameter  $\eta$  can be iteratively adjusted to provide the expected goodness-of-fit. Note that the ME regularization ensures that the reconstructed surface mass distribution is positive definite.

## 2.4 The ellipticity distribution

Given the intrinsic ellipticity distribution and the local values of  $\kappa$  and  $\gamma$ , the probability distribution  $p(\chi)$  for the image ellipticities can be calculated. However, the resulting analytic expressions are quite cumbersome and unsuitable for the high-dimensional minimization problem considered here. With the intrinsic distribution not being accurately known anyway, a precise expression of  $p(\chi)$  is not needed. We therefore approximate the image ellipticity distribution by a Gaussian, with mean  $\langle\chi\rangle$  and dispersion  $\sigma_\chi$ . Both these values depend on the (local) distortion,

$$\delta = \frac{2g}{1 + |g|^2}, \quad (10)$$

where  $g = \gamma/(1 - \kappa)$  is the reduced shear. Mean and dispersion can be approximated by (Schneider & Seitz 1995)

$$\begin{aligned} \langle\chi\rangle &= \zeta \delta \equiv \left[1 - \frac{M_2}{2} (1 - |\delta|^2)^{\mu_1}\right] \delta, \\ \sigma_\chi &= \sigma_0 (1 - |\delta|^2)^{\mu_2}, \end{aligned} \quad (11)$$

where

$$\mu_1 = 1 - \frac{3M_4}{4M_2}, \quad \mu_2 = \frac{6M_2 + M_2^2 - 9M_4}{8M_2}, \quad (12)$$

and  $M_n$  is the  $n$ -th moment of the intrinsic ellipticity distribution. Using (5) and (7), the function  $E$  to be minimized can then be written

$$E(\{\psi\}) = G_\chi(\{\psi\}) + \sum_{k=1}^{N_g} \ln[\sigma_\chi^2(k)] + \eta \mathcal{R}(\{\psi\}), \quad (13)$$

where we have introduced

$$G_\chi := \frac{1}{N_g} \sum_{k=1}^{N_g} \frac{|\chi_k - \langle\chi\rangle(k)|^2}{\sigma_\chi^2(k)}. \quad (14)$$

$\langle\chi\rangle(k)$  and  $\sigma_\chi(k)$  are the values of  $\langle\chi\rangle$  and  $\sigma_\chi$  at the position of the  $k$ -th galaxy, which obviously depend on the deflection potential  $\{\psi\}$  through the distortion  $\delta$ .<sup>1</sup> The term  $G_\chi$  in  $E$  has the form of a  $\chi^2$ -function, which implies that an acceptable mass model should have  $G_\chi \approx 1$ . This condition constrains the regularization parameter  $\eta$ .

We outline in the Appendix an efficient method for calculating  $E$  and its derivatives with respect to the values of  $\psi$  on the grid points. We note that the terms in the sums of (13) and (14) corresponding to a galaxy at  $\bar{\theta}_k$  depend only on the values of  $\psi$  at neighboring grid points. In that sense, our method is local. Had we parameterized the cluster by  $\kappa$  at grid points, each term in the sums depended on  $\kappa$  at all grid points, as can be seen from (3). It becomes obvious that the description in terms of  $\psi$  requires much less computer time. In addition, the use of  $\kappa$  rather than  $\psi$  is strongly disfavored by the fact that the shear on  $\mathcal{U}$  is incompletely specified by  $\kappa$  on the same field. Bridle et al. (1998) attack this problem by performing the reconstruction on a region much larger than  $\mathcal{U}$ . They find that the shear information within  $\mathcal{U}$  yields information about  $\kappa$  outside  $\mathcal{U}$ . Although this is true, the information on the mass outside the data field

<sup>1</sup>If we worked in terms of the ellipticity parameter  $\epsilon$  (see BBNS) rather than the ellipticity  $\chi$ , then  $\langle\epsilon\rangle = g$  (Seitz & Schneider 1997) for a non-critical cluster. In the general case including critical clusters, the variable  $\chi$  is more convenient.

is *very* limited: For a circular data field, the shear inside  $\mathcal{U}$  caused by mass outside  $\mathcal{U}$  can be fully described by conveniently defined multipole moments of the mass distribution outside  $\mathcal{U}$  (Schneider & Bartelmann 1997), and there are infinitely many mass distributions for which all of those multipole moments agree. For instance, a point mass located just outside the data field produces the same shear pattern in the field as a spherically symmetric mass distribution with the same total mass. Finally, extending the region on which the reconstruction is performed increases the dimensionality of the minimization problem.

## 2.5 Including magnification information

The mass-sheet degeneracy (6) can be lifted if the lens magnification can be estimated. Three different methods for measuring magnification were suggested in the literature. Broadhurst et al. (1995) proposed to use the magnification bias, which changes the local number density of background galaxies due to the magnification, provided the slope of the number counts  $d \log N/dm$  is sufficiently different from 0.4. Noting that lensing magnifies objects but leaves their surface brightness unchanged, Bartelmann & Narayan (1995) suggested that the sizes of background galaxies at fixed surface brightness could be a convenient measure for the magnification after calibrating with field galaxies. Both methods can be used locally or globally. In the first case, the local magnification information is used for the mass reconstruction, whereas in the latter case, the transformation parameter  $\lambda$  in (6) is adjusted until the magnification optimally matches the observational estimate. Kolatt & Bartelmann (1998) suggested to calibrate  $\lambda$  globally by using type-Ia supernovae as cosmological standard candles. If magnification information is taken into account, the potential  $\psi$  can be kept fixed at three points only, yielding  $N_{\text{dim}} = (N_x + 2)(N_y + 2) - 7$ .

As an example, consider the method suggested by Bartelmann & Narayan (1995). Let  $r^s$  and  $r$  be the ratios of the linear sizes of a galaxy and its image, respectively, relative to the mean size of galaxies with the same surface brightness. They are related by  $r = |\mu|^{1/2} r^s$ . The expectation values of  $r^s$  and  $r$  are 1 and  $|\mu|^{1/2}$ , respectively. Hence, if  $\hat{p}_s(r^s)$  is the probability distribution for  $r^s$ , the local probability distribution for  $r$  is

$$\hat{p}(r) = |\mu|^{-1/2} \hat{p}_s\left(|\mu|^{-1/2} r\right). \quad (15)$$

Including the size distribution into the likelihood maximization leads to an additional term in (13),

$$\begin{aligned} E(\{\psi\}) &= G_\chi(\{\psi\}) + \frac{1}{2} G_r(\{\psi\}) \\ &+ \sum_{k=1}^{N_g} \ln[\sigma_\chi^2(k)] + \eta \mathcal{R}(\{\psi\}), \end{aligned} \quad (16)$$

where

$$G_r := \frac{2}{N_g} \sum_{k=1}^{N_r} |\mu(k)|^{-1/2} \hat{p}_s\left(|\mu(k)|^{-1/2} r(k)\right). \quad (17)$$

We assume  $\hat{p}_s$  to be a log-normal distribution (cf. Bartelmann & Narayan 1995),

$$\hat{p}_s(\ln r^s) = \frac{1}{\sqrt{2\pi}\sigma_r} \exp\left[-\frac{(\ln r^s + \sigma_r^2/2)^2}{2\sigma_r^2}\right], \quad (18)$$

with  $\langle r^s \rangle = 1$ , and (17) becomes

$$G_r := \frac{1}{N_g} \sum_{k=1}^{N_r} \frac{[\ln r(k) - \langle \ln r \rangle(k)]^2}{\sigma_r^2}, \quad (19)$$

with  $\langle \ln r \rangle(k) = (\ln |\mu(k)| - \sigma_r^2)/2$ . Hence,  $\hat{p}$  is a Gaussian in  $\ln r$ , with dispersion  $\sigma_r$ .  $G_r$  has the form of a  $\chi^2$  function in  $\ln r$ , which motivates us to include the factor 1/2 in the definition of  $G_r$ . A satisfactory mass model should have  $G_r \approx 1$ . Note that the galaxies whose size can reliably be measured need not be those used for measuring the shear. It is just for notational simplicity that we assume that the two galaxy populations agree.

### 3 Practical implementation and simulation parameters

#### 3.1 Practical implementation

For minimizing (13) or (16) in the process of the ML mass reconstruction, the various quantities (e.g.  $\langle \chi \rangle(k)$ ,  $\sigma_\chi(k)$ ,  $\hat{\kappa}_{ij}$ ) need to be calculated for each set of values  $\{\psi\}$  of the deflection potential. We outline in the Appendix how this can be done efficiently. In order to quickly approach the minimum of  $E$ , we use derivative information in the minimization procedure. The derivative of  $E$  with respect to  $\psi_{ij}$  is also given in the Appendix. We employ the conjugate gradient method as encoded in the routine `frprmn` by Press et al. (1992), with line minimization using derivative information.

We need a good initial potential to start the minimization. We tested two different approaches. The first starts with a relatively small grid (say,  $N_x = N_y = 11$  for a quadratic data field  $\mathcal{U}$ ), and a potential which corresponds to a constant surface mass density of  $\kappa \approx 0.1$ , say.  $\eta$  can be set to zero initially because the large grid cells provide sufficient smoothing to avoid over-fitting the data, or otherwise set  $\eta$  to a small value with a constant prior. After several (20, say) iterations, the current mass map is smoothed and used as the new prior, and the minimization is continued. The regularization parameter is slightly increased or decreased, depending on whether  $G_\chi$  is smaller or larger than unity. Once a stable minimum with  $G_\chi \approx 1$  is obtained, the solution can be interpolated to a finer grid ( $N_x = N_y = 21$ , say) and the minimization can continue, adapting the prior and the regularization parameter as described before. This procedure can be repeated if desired.

The second approach starts on a fine grid right away, with initial conditions obtained from a direct finite-field reconstruction method like that described by Seitz & Schneider (1998). From this mass distribution, an approximate deflection potential can be found by integration, although any contribution from the mass outside the data field will be missing in the resulting  $\psi$ . This initial prior is a smoothed version of the mass map from the direct reconstruction, and is adapted as described above. If there is no mass concentration directly outside the data field, the second method converges faster, while the first approach should be used if the data field does not encompass most of the mass concentration. Of course, both methods finally approach solutions with  $G_\chi \approx 1$ . If magnification information is available,  $G_r$  should finally approximate unity, which provides a useful consistency check of the result.

#### 3.2 Simulation parameters

We carry out simulations in which background galaxies are lensed by the mass model shown in Fig. 1. It consists of two softened isothermal spheres, with parameters chosen such that the lens is sub-critical. We successfully performed simulations with critical clusters as well, but concentrate on the non-critical case to simplify comparisons with the noise-filter reconstructions of Seitz & Schneider (1996). The modifications to the practical implementation necessary for critical clusters are given in the Appendix. The data field  $\mathcal{U}$  is a square with side length  $5'$ . We choose a number density of 50 galaxies per square arc minute, approximately corresponding to the number density which can be achieved with several hours exposure time at a four-meter class telescope in good seeing. All reconstructions were performed on a grid with  $N_x = N_y = 41$ . Note that the parameters are chosen such that the grid cells have about the same size as the mean separation

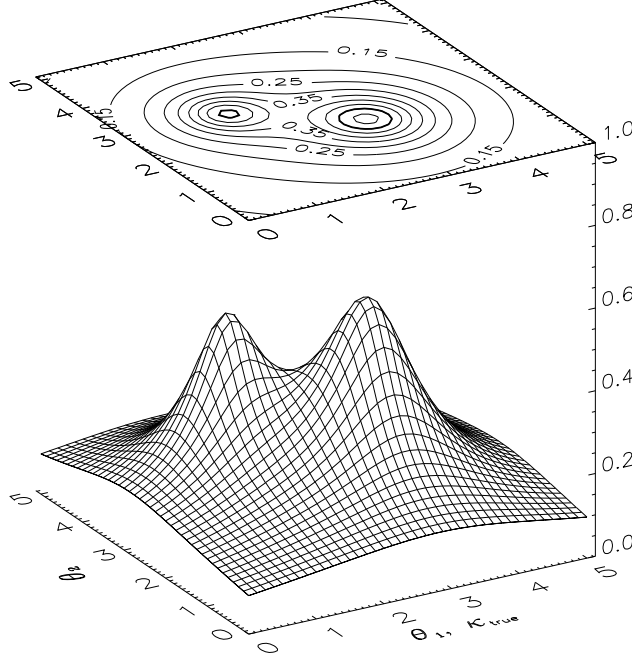


Figure 1: A mass model consisting of two softened isothermal spheres with core sizes 0.6 and 0.8, and central surface mass densities  $\kappa_c = 0.4$  and  $0.5$ , respectively. Contours are spaced by  $0.05$ , and the heavy contour follows  $\kappa = 0.5$

between galaxies. The intrinsic ellipticity distribution was chosen to be approximately Gaussian,

$$p_s(\chi^s) = \frac{1}{\pi R^2 [1 - \exp(-1/R^2)]} \exp(-|\chi^s|^2 / R^2), \quad (20)$$

with  $R = 0.3$ , yielding  $M_2 \approx 0.09$ ,  $\mu_1 \approx 0.87$ , and  $\mu_2 \approx 0.55$  in (11) and (12). The distribution  $\hat{p}_s$  of relative source sizes is characterized by  $\sigma_r = 0.5$  (see Bartelmann & Narayan 1995 for a discussion of this choice). The “observed” ellipticities and relative source sizes are calculated from realizations of the source distributions, using the gravitational lens equations.

In order to assess the expected deviation of  $G_\chi$  and  $G_r$  from unity, we plot in Fig. 2 the quantities

$$\begin{aligned} G_\chi(<\beta) &:= \left\langle \frac{|\chi_k - \langle \chi \rangle(k)|^2}{\sigma_\chi^2(k)} \right\rangle_{|\bar{\theta}_k| < \beta}, \\ G_\chi(\beta) &:= \left\langle \frac{|\chi_k - \langle \chi \rangle(k)|^2}{\sigma_\chi^2(k)} \right\rangle_{\beta - \Delta\beta \leq |\bar{\theta}_k| < \beta}, \\ G_r(<\beta) &:= \left\langle \frac{[\ln r(k) - \langle \ln r \rangle(k)]^2}{\sigma_r^2} \right\rangle_{|\bar{\theta}_k| < \beta}, \\ G_r(\beta) &:= \left\langle \frac{[\ln r(k) - \langle \ln r \rangle(k)]^2}{\sigma_r^2} \right\rangle_{\beta - \Delta\beta \leq |\bar{\theta}_k| < \beta}. \end{aligned} \quad (21)$$

They are the contributions to  $G_\chi$  and  $G_r$  from galaxies closer than  $\beta$  to the center of the data field, or within rings of width  $\Delta\beta = 0.25$  around the center of the data field. Fig. 2 shows that the quantities (21) vary considerably between realizations, owing to the broad distribution of

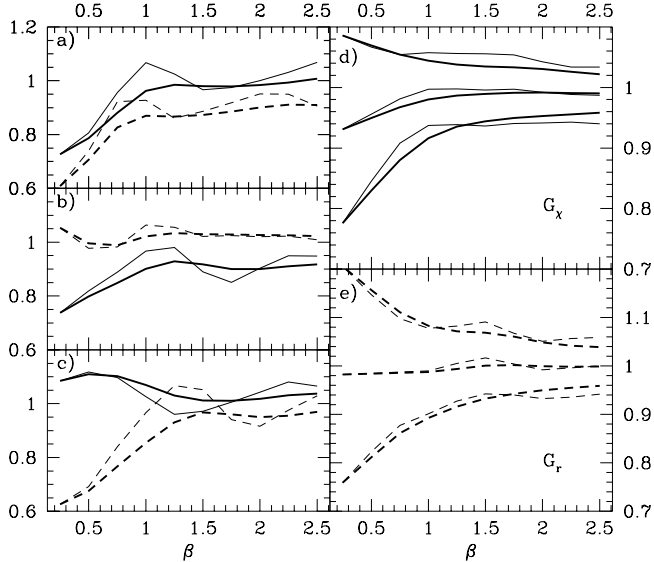


Figure 2: Panels (a) through (c) show the chi-square contributions of the observables, viz. ellipticity and image size, within circles of radius  $\beta$ , and within rings of outer radius  $\beta$  and width  $\Delta\beta = 0.25$ , for three different realizations of the source population. For this figure, the true mass distribution of the lens was taken, so that these curves merely show the noise properties of the source population. Heavy solid curves:  $G_\chi(< \beta)$ ; light solid curves:  $G_\chi(\beta)$ ; heavy dashed curves:  $G_r(< \beta)$ ; light dashed curves:  $G_r(\beta)$ . Panels (d) and (e) show the average of these four quantities, obtained from 50 realizations of the source population, together with their 1- $\sigma$ -variations, shown by the same line types

intrinsic source properties. When averaged over 50 realizations (Figs. 2d,e), their mean values are very close to unity, and their 1- $\sigma$  variations are a good indicator for the expected values in true reconstructions.

Even when the exact deflection potential is used, the resulting mass distribution  $\kappa$  will deviate from the true surface mass density because  $\kappa$  is calculated from  $\psi$  with finite differencing. For the mass distribution shown in Fig. 1,  $\kappa$  from finite differencing deviates from the true  $\kappa$  by  $\lesssim 0.03$  everywhere, with the largest deviations occurring at the two mass peaks. The grid is too coarse for a more accurate calculation of the second-order derivatives. Since the deviations are sufficiently small (i.e. much smaller than the expected accuracy that we can hope to achieve from our reconstruction), we have chosen not to further refine the grid. It should be noted that the method by Bridle et al. (1998) suffers from the same, or worse, inaccuracies, because there the shear is calculated from the surface mass density by integrating over a coarse grid.

Finally, Bridle et al. (1998) calculated the covariance matrix for the resulting mass distribution, which we do not repeat here. One must take into account, though, that the error estimates of the resulting mass reconstruction are strongly correlated, because the shear depends non-locally on  $\kappa$ .

## 4 Results

### 4.1 ML reconstructions without magnification information

We first neglect magnification information, i.e. we minimize (13). For the mass model in Fig. 1, mass reconstructions for 50 realizations of the galaxy population were performed. For each realization, 1000 iterations were taken, in each case using the noise-filter reconstruction of Seitz & Schneider (1996) as initial potential. The number of iterations was chosen to produce a stable result for all realizations. The actually required number can be substantially smaller in individual cases. Typically, 1000 iterations take approximately 30 minutes on an IBM 590 workstation. After every 20 iterations, the prior was changed to the current mass distribution, smoothed by a Gaussian of width  $\theta_{\text{sm}} = 0.2$  for the first 600 iteration steps, and  $\theta_{\text{sm}} = 0.15$  afterwards. A somewhat larger smoothing length at the beginning leads to faster convergence, but produces artifacts due the finite region over which the integral in (3) is performed. Note that  $\theta_{\text{sm}}$  is of the same size as the grid cells. In order to avoid excessive fine-tuning for these simulations, the regularization

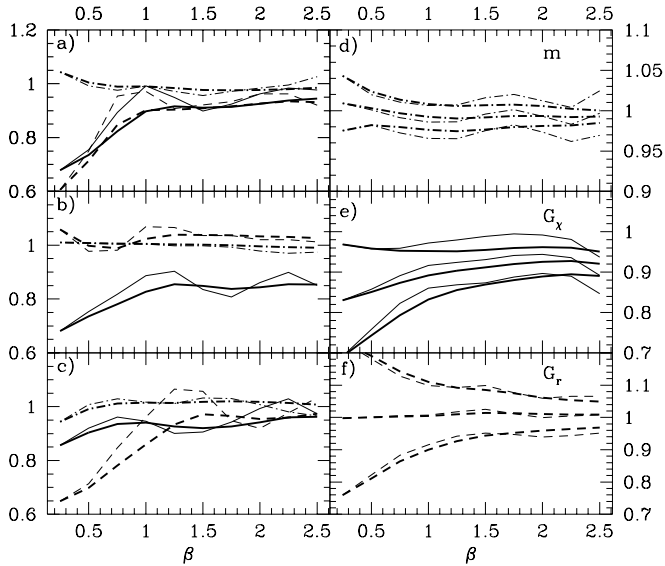


Figure 3: Panels (a) through (c) show the chi-square quantities (21), together with the mass ratios (22) for the reconstructions obtained from three different realizations of the galaxy population. Heavy solid curves:  $G_\chi(< \beta)$ ; light solid curves:  $G_\chi(\beta)$ ; heavy dashed curves:  $G_r(< \beta)$ ; light dashed curves:  $G_r(\beta)$ ; heavy dash-dotted curves:  $m(< \beta)$ ; light dash-dotted curves:  $m(\beta)$ . In panels (d) through (f), the average of these quantities from 50 realizations are displayed together with their  $1\text{-}\sigma$  range (shown by the same line types). For these simulations, the regularization parameter was kept constant, i.e. not adjusted for each simulation to yield  $G_\chi \approx 1$ . No magnification information was used

parameter  $\eta$  was fixed to  $\eta = 30$  for all 50 realizations. Of course  $\eta$  could be changed to finally achieve  $G_\chi = 1$  for each individual realization. The current choice of  $\eta$  was made to achieve  $G_\chi \approx 1$  for all realizations (see Fig. 3 below). The final 20 iteration steps were performed with a value of  $\eta$  large enough to make the mass distribution follow the prior very closely, and which yields a smoothing of the mass reconstruction on a scale of  $\theta_{\text{sm}}$ .

Since no magnification information was used in these simulations, the resulting deflection potential (and thus the mass distribution) is determined only up to the mass-sheet transformation (6). In order to compare the reconstructions with the input model, each mass map was transformed such that the total mass inside  $\mathcal{U}$  agreed with the true total mass. In Fig. 3, we show the quantities (21) for three different realizations of the galaxy population, together with the ratios

$$\begin{aligned}
 m(\beta) &:= \frac{M(\beta)}{M_{\text{true}}(\beta)}, \\
 m(< \beta) &:= \frac{M(< \beta)}{M_{\text{true}}(< \beta)}
 \end{aligned}
 \tag{22}$$

of the reconstructed mass inside rings and circles, relative to the true mass distribution. As can be seen, these mass ratios are always very close to unity, which means that the mass maps are reconstructed with high accuracy (up to the mass-sheet degeneracy). The dispersion of  $m(\beta)$  about unity is less than 5%, and the mean of  $m(\beta)$  over 50 realizations is astonishingly flat. There is no indication that the mass at the center or in the outer parts is systematically over- or underestimated. The choice of the regularization parameter results in  $G_\chi$  being slightly smaller than unity on average, though with substantial variation from case to case. Evidently,  $G_\chi(\beta)$  is significantly smaller in the inner part than in the outer part, an effect also seen in Fig. 2 where the true mass distribution was considered. This is due to the fact that the ellipticity distribution after lensing is not really a Gaussian, and the deviation from this assumed functional form becomes larger for larger values of the reduced shear, i.e. closer to the center of  $\mathcal{U}$ . Whereas there is no fundamental difficulty in replacing the Gaussian with a more accurate probability distribution, the simple form for  $G_\chi$  is computationally convenient and seems to be sufficiently accurate for the mass reconstructions, as seen from the dash-dotted curves in Fig. 3. The deviation of  $G_r(\beta)$  from unity can be substantial in individual reconstructions, but the mean over all realizations is very close to unity.

At the edge of the data field, two systematic effects become visible in the mean quantities

plotted in Figs. 3d–f (and also by looking at the 2-d distribution over  $\mathcal{U}$ ): The value of  $G_\chi(\beta)$  shows a small but significant decrease, and  $\kappa$  is slightly too large near the boundary. The first of these effects can be understood by considering the number of galaxies for which the shear estimate is affected if the value of  $\psi$  is changed at a grid point. If that grid point is located in the inner part of  $\mathcal{U}$ , the estimates of  $\gamma$  for galaxies within the neighboring 16 grid cells are affected. This number decreases for points near the boundary of  $\mathcal{U}$ , so that  $\psi$  there is less constrained by the measured image ellipticities. This implies that at the boundary, it is easier to “fit the noise” caused by the intrinsic ellipticity distribution. The slightly too large  $\kappa$  near the boundary is due to the prior. The prior is obtained from local averaging of the current mass distribution. If the mass distribution decreases outwards, the local mean value which can only be taken from the grid points within  $\mathcal{U}$  will be slightly too large at the boundary, which explains why the method presented here is slightly biasing the mass map at the boundary. In actual applications, a strip of width  $\theta_{\text{sm}}$  can be ignored in the analysis of the mass distribution if this bias is a worry. However, its amplitude is very small, and it can probably be safely ignored in most situations compared to the stochastic errors. Alternatively, one can use a mild extrapolation of the smoothed mass distribution to obtain an estimate of the smoothed  $\kappa$  values on the boundary less affected by this bias. In the case of our mass model, a simple fix (instead of a more elaborated extrapolation) can be obtained by decreasing  $\kappa$  by  $\Delta\kappa = 0.0015$  on all boundary points, which practically eliminates the bias. We use this simple fix to the simulations discussed in the next subsection. We further point out that the amplitude of this mass bias can also be checked with real data, by generating artificial data sets from the reconstructed mass distribution and by performing reconstructions for those in the same way in which the original mass reconstruction was obtained.

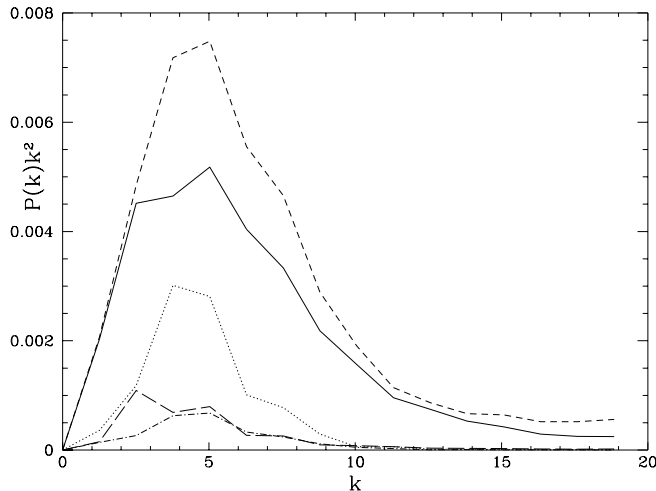


Figure 4: Power spectra  $k^2 P(k)$  of the difference between the values of  $K(\vec{\theta}) = \ln[1 - \kappa(\vec{\theta})]$  from reconstructed mass distributions and the true mass distribution (see Seitz & Schneider 1996 for a definition of  $P(k)$  and its practical calculation). The solid curve corresponds to  $K_{\text{ML}}$ , the short-dashed curve to  $K_{\text{NF}}$ . In addition, we plot the power spectra of the difference between the ensemble-averaged mass maps, both from the ML method (long-dashed curve) and the noise-filter reconstruction (dotted curve). For comparison, the dash-dotted curve shows the power spectrum of the difference obtained from the finite-differencing error, mentioned at the end of Sect. 3

The mass-sheet transformation (6) allows to determine the quantity  $K(\vec{\theta}) = \ln[1 - \kappa(\vec{\theta})]$  up to an additive constant. As in Seitz & Schneider (1996, 1998; SK), we perform a power-spectrum analysis of the difference between  $K_{\text{ML}}$  and  $K_{\text{true}}$ , i.e. between the  $K$  from the ML reconstructions and from the true mass distribution. Note that this power spectrum for  $k \neq 0$  is independent of the transformation (6). In Fig. 4, we compare the power spectrum obtained from our 50 realizations to the power spectrum obtained from the difference between  $K_{\text{NF}}$  and  $K_{\text{true}}$ , the former one corresponding to the noise-filter mass reconstruction of Seitz & Schneider (1996), using

the same realizations of the galaxy population. As can easily be seen, the ML reconstruction yields substantially lower values for  $P(k)$  than the noise-filter reconstruction.

For illuminating the main reason for this difference, we also calculate the power spectra of the difference between  $\langle K_{\text{ML}} \rangle$ ,  $\langle K_{\text{NF}} \rangle$  and  $K_{\text{true}}$ , the former two being the mean reconstructed mass distribution averaged over all 50 realizations. The difference between these two power spectra is very large, with the power of  $\langle K_{\text{NF}} \rangle - K_{\text{true}}$  being much larger than for the ML reconstructions. Almost the entire difference comes from the inability of the noise-filter method to resolve the core of the two mass peaks in the model appropriately because of the unavoidable smoothing. Note that the smoothing scale  $\Delta\theta$  in the noise-filter reconstruction is much larger than the smoothing scale  $\theta_{\text{sm}}$  for the prior in the ML method, the latter being of the same order as the size of a grid cell, or the mean separation between two background galaxy images, which in any case is smallest scale one can hope to resolve. In fact, it seems that the power spectrum of  $K_{\text{NF}} - K_{\text{true}}$  is approximately the sum of the power spectra of  $K_{\text{ML}} - K_{\text{true}}$  and  $\langle K_{\text{NF}} \rangle - K_{\text{true}}$ . In other words, the error of the noise-filter reconstruction is due to a systematic error (from smoothing, although it is adaptive smoothing as in Seitz & Schneider 1996), and a stochastic error which is approximately the same as that for the ML reconstruction.

The power spectrum of the error resulting from finite differencing is shown as the dash-dotted curve in Fig. 4 and is seen to be about the same as that of  $\langle K_{\text{ML}} \rangle - K_{\text{true}}$ . I.e., the largest part of the error of the mean mass map in the ML reconstruction comes from finite differencing; only for  $k \leq 3$  is the latter error larger than that from finite differencing. This little power excess is due to the aforementioned slight bias at the boundary of  $\mathcal{U}$ .

To conclude this subsection, we have shown that the ML method yields more accurate mass reconstructions than the noise-filter method, whereby the largest difference is due to the better angular resolution of the ML method in those parts of the data field where the data require more local structure, whereas the noise-filter method – like all direct methods developed so far – uses a fixed smoothing scale, or at best an ad-hoc choice for the change of smoothing scale with the signal, such as in Seitz et al. (1996, and references therein). The ML mass distributions are slightly biased at the boundary of the data field, and the amplitude of this bias depends on the mass distribution.

## 4.2 ML reconstructions with magnification information

For the 50 realizations of the background galaxies, we also performed ML mass reconstructions including magnification information, i.e. minimizing (16). Each reconstruction proceeded as described in the beginning of Sect. 4.1, except that the regularization parameter was chosen to be  $\eta = 60$  instead of 30. This is necessary to give the regularization the same weight as before, because the chi-square part of  $E$  is now effectively doubled. The number of iteration steps was slightly increased to 1200. Anticipating that the additional magnification information would allow a slightly higher angular resolution of the mass map, we somewhat reduced the smoothing scale for the prior to  $\theta_{\text{sm}} = 0.1$ .

In analogy to Fig. 3, we plot in Fig. 5 the quantities (21) and (23) for three different realizations of the galaxy population, their average over 50 realizations, and their dispersion. Comparing the two figures, it seems that including magnification information does not change the curves significantly, apart from the fact that the mass-sheet transformation is now obsolete. Magnification information therefore mainly affects the normalization of the mass map, but does not provide significant information on its shape.

To further illustrate this point, we plot in Fig. 6 the power spectra of the difference between reconstructed mass maps  $K_{\text{ML}}$  and the model mass distribution  $K_{\text{true}}$ , similar to Fig. 4. The difference in the power spectra between reconstructions with and without magnification information is much smaller than their difference to the noise-filter mass reconstructions, at least for small values of  $k \lesssim 7$ . For larger  $k$ , the difference becomes somewhat larger, but this may simply be due to the different choice of the regularization parameter which affects the small-scale noise. In our model, these small scales are only noise because the mass model is relatively smooth. The power spectra of the ensemble-averaged mass maps show that the spectrum for simulations with magni-

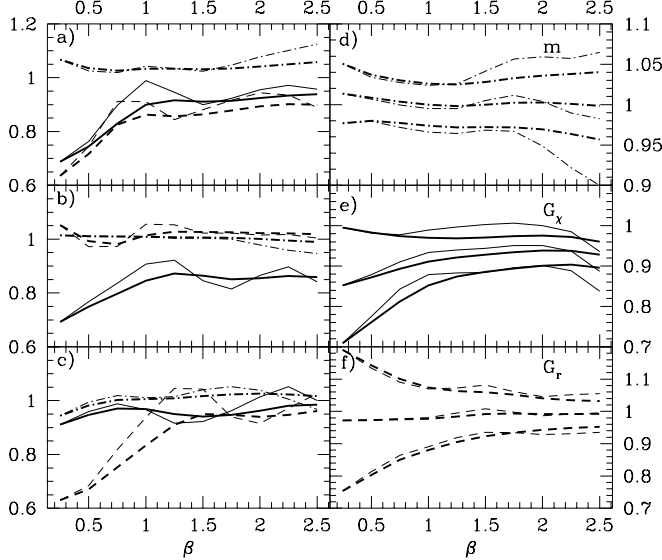


Figure 5: In analogy to Fig. 3, we plot in panels (a) through (c) the chi-square contributions (21), together with the mass ratios (22), for the ML-reconstructions obtained from three different realizations of the galaxy population, now using magnification information. Heavy solid curves:  $G_\chi(< \beta)$ , light solid curves:  $G_\chi(\beta)$ ; heavy dashed curves:  $G_r(< \beta)$ ; light dashed curves:  $G_r(\beta)$ ; heavy dash-dotted curves:  $m(< \beta)$ ; light dash-dotted curves:  $m(\beta)$ . In panels (d) through (f), the average of these quantities over 50 realizations is displayed together with their  $1\text{-}\sigma$  range. For these simulations, the regularization parameter was kept constant, i.e. not adjusted for each simulation to achieve  $G_\chi \approx 1$

magnification information is somewhat lower. This is probably due to the fact that the magnification information leads to a slightly better angular resolution in the core of the two mass concentrations.

Our simulation results therefore allow to conclude that magnification information does not contribute much information on the *shape* of the mass distribution compared to shear information. For estimating the relative accuracy of the mass determination, one can then assume that the mass map is known from the galaxy shapes up to the mass-sheet transformation. Let  $\kappa$  be the true mass distribution and  $\kappa(\lambda)$  the distribution transformed with (6). The magnification information can then be used to determine  $\lambda$  such as to best fit the galaxy sizes, i.e. to minimize  $G_r$ . Noting that (6) transforms magnifications like  $\mu \rightarrow \mu/\lambda^2$ , the best-fitting  $\lambda$  is

$$\ln \lambda = -\frac{1}{N_g} \sum_{k=1}^{N_g} \left[ \ln r(k) - \left| \mu(\vec{\theta}_k) \right|^{1/2} \right]. \quad (23)$$

Since the distribution of the  $\ln r$  is Gaussian, the values of  $\ln \lambda$  for different realizations of the galaxy population follow a Gaussian probability distribution with zero mean and dispersion  $\sigma_\lambda = \sigma_r/\sqrt{N_g}$ . Whereas the distribution of  $\ln \lambda$  is symmetric about zero, the mean of  $\lambda$  is not unity. The ratio

$$m(\lambda) = \frac{M(\lambda)}{M} = \frac{\langle \kappa(\lambda) \rangle}{\langle \kappa \rangle} = \frac{1}{\langle \kappa \rangle} + \lambda \left( 1 - \frac{1}{\langle \kappa \rangle} \right) \quad (24)$$

of the estimated mass to the true mass has a median of unity, but a slightly smaller mean,

$$\begin{aligned} \langle m \rangle &= \int_{-\infty}^{\infty} d \ln \lambda p(\ln \lambda) m(\ln \lambda) \\ &\approx 1 - \left( \frac{1}{\langle \kappa \rangle} - 1 \right) \frac{\sigma_r^2}{2N_g}. \end{aligned} \quad (25)$$

The deviation of  $\langle m \rangle$  from unity is very small: For  $N_g = 1250$  and  $\sigma_r = 0.5$ , and a mass model with  $\langle \kappa \rangle \approx 0.2$ , we find  $\langle m \rangle \approx 0.9996$ . Similarly, the dispersion of  $m$  is

$$\sigma_m = \sqrt{\langle m^2 \rangle - \langle m \rangle^2} \approx \left| \frac{1}{\langle \kappa \rangle} - 1 \right| \frac{\sigma_r}{\sqrt{N_g}}, \quad (26)$$

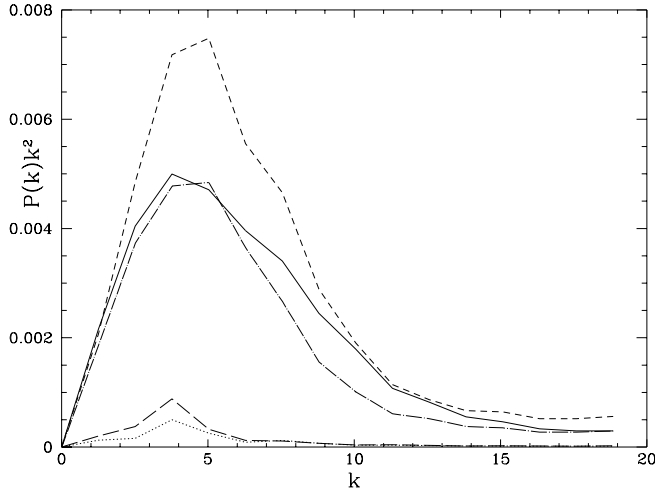


Figure 6: Power spectra  $k^2 P(k)$  of the difference between the reconstructed mass distributions  $K(\vec{\theta}) = \ln[1 - \kappa(\vec{\theta})]$  and the true mass distribution. The solid and long-dash-dotted curves show  $K_{\text{ML}}$  obtained without and with magnification information, respectively. For comparison, the short-dashed curve shows  $K_{\text{NF}}$ . In addition, we plot the power spectra of the difference between the ensemble-averaged mass distributions, both from the ML method without (long-dashed curve) and with (dotted curve) magnification information

where we have used  $\sigma_r/\sqrt{N_g} \ll 1$  in the approximations. For the same parameters as before,  $\sigma_m = 0.057$ . We therefore expect that our mass model can be reconstructed with an accuracy of about 6% if the shape of the mass distribution is sufficiently constrained by image shapes. Fig. 5d shows that this estimate is in very good agreement with the mass estimate obtained from the ML reconstruction using the magnification information.

To elaborate on this point, we plot in Fig. 7 the ratios of four different mass estimates to the true mass. These are: the mass from ML reconstructions (i) with and (ii) without magnification information, but transformed according to (23) to best fit the source sizes; (iii) mass-sheet-transformed noise-filter reconstructions; and (iv) the mass-sheet-transformed true density distribution. Obviously, the scatter of the mass estimates across the four different methods is very much smaller than that caused by different realizations of the source population. As much as 50 realizations allow to conclude, all four methods yield an unbiased estimate of the total mass and have approximately the same dispersion, close to the theoretical expectation discussed above.

We investigated how the quality of mass estimates is affected by the spatial resolution. The noise-filter reconstructions have a lower resolution than the ML reconstructions, although our adaptive smoothing makes them satisfactorily resolve the mass peaks. We performed noise-filter reconstructions with fixed smoothing scales of 0.3 and 0.5. In those cases, the peaks are fairly much smoothed out. Applying then (23) to match image sizes, we found that the total mass within  $\mathcal{U}$  is systematically overestimated, by  $\sim 1\%$  and  $\sim 3\%$ , respectively. This is because the smoothing of the map renders the model magnification too low to match the observed high magnifications close to mass peaks, for which the invariance transformation tends to compensate with a slightly higher mass. This bias also affects the ML reconstruction of BNSS because of missing resolution in the cluster center. However, it is sufficiently small to be not of much practical importance for reconstructions which can be expected from real data in the near future, but it should be kept in mind if a large sample of clusters is investigated statistically.

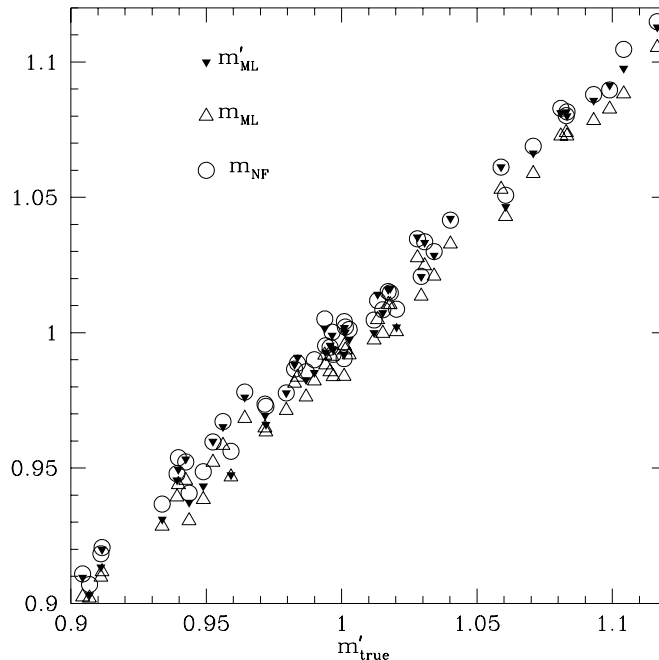


Figure 7: For 50 realizations of the galaxy population, we estimate the total mass inside  $\mathcal{U}$  and compare it to the true mass. Defining  $m := M/M_{\text{true}}$ , we plot (i) the mass ratio  $m_{\text{ML}}$  obtained from ML reconstructions including magnification information, (ii) the ratio  $m'_{\text{ML}}$  obtained from ML reconstructions without magnification information, but mass-sheet transformed according to (23), and (iii) the mass ratio  $m_{\text{NF}}$  obtained from noise-filter reconstructions, transformed according to (23), against (iv) the ratio  $m'_{\text{true}}$  obtained from the true shape of the mass distribution, also invariance transformed according to (23). The means and dispersions of the four mass ratios are: (i)  $\langle m_{\text{ML}} \rangle = 0.994$ ,  $\sigma_m = 0.051$ ; (ii)  $\langle m'_{\text{ML}} \rangle = 1.000$ ,  $\sigma_m = 0.052$ ; (iii)  $\langle m_{\text{NF}} \rangle = 1.002$ ,  $\sigma_m = 0.051$ ; and (iv)  $\langle m'_{\text{true}} \rangle = 1.001$ ,  $\sigma_m = 0.054$ . Within the accuracy allowed by 50 realizations, they all agree with  $\langle m \rangle = 1$  and  $\sigma_m \approx 0.052$ , very much in agreement with the estimate (26)

## 5 Discussion and conclusions

We presented a new method for reconstructing projected mass distributions of galaxy clusters. The method uses image distortions of background galaxies and their size as a function of surface brightness. Our entropy-regularized ML method (Seitz 1997) is a further development of previously published inverse methods for the mass reconstruction. In particular, we describe the lens by its deflection potential  $\psi$  as suggested by BNSS. This is of major importance, for two reasons. First, if the surface mass density  $\kappa$  on a finite field  $\mathcal{U}$  is used to describe the lens, the shear on  $\mathcal{U}$  is incompletely specified by the model because the mass distribution outside  $\mathcal{U}$  can contribute to the shear. Second, the shear at the position of any galaxy depends only locally on  $\psi$ , which allows a much faster minimization algorithm for a given number of grid points.

We regularize the method by an entropy term as suggested by Bridle et al. (1998), but additionally adapt the prior to the current model of the mass distribution. This ‘moving prior’ (Lucy 1994) allows a considerably higher resolution of mass peaks. The spatial resolution of the entropy-regularized ML method adapts itself to the strength of the lensing signal, producing mass distributions which are as smooth as possible, and as structured as the data require. In that respect, our method differs from that of BNSS and SK. We showed that the ML method is superior to the noise-filter method (Seitz & Schneider 1996) which was the most accurate of the presently

known direct inversion methods (Seitz & Schneider 1996, 1998; SK; Lombardi & Bertin 1998).

Obviously, the method described here is not restricted to rectangular data fields, but can easily be adapted to any geometry of  $\mathcal{U}$  by covering  $\mathcal{U}$  with quadratic grid cells, and adding a boundary of grid points for  $\psi$  – the rest is only a matter of labeling. Furthermore, we note that observational errors can be incorporated into the likelihood function. For example, if the measurement error of the ellipticity  $\chi$  is  $\sigma_{\text{obs}}$ , one can replace  $\sigma_\chi^2$  in (13 and 14) by  $\sigma_\chi^2 + \sigma_{\text{obs}}^2$ .

In contrast to the direct inversion methods, all of which are variants and generalizations of the original Kaiser & Squires (1993) method, the inverse methods allow to include additional information on top of the shear measured through image ellipticities. We demonstrated this here by adding magnification information derived from image sizes at given surface brightness, as discussed by Bartelmann & Narayan (1995). However, we could equally well use the change of number counts due to magnification bias (Broadhurst et al. 1995) as an additional constraint. In that case, if the number counts of a certain (e.g. color-selected) galaxy population have a cumulative slope of  $-\beta$ , the expected number density of background galaxies at a position  $\vec{\theta}$  is  $n(\vec{\theta}) = n_0 \left| \mu(\vec{\theta}) \right|^{\beta-1}$ , where  $n_0$  are the counts at the same flux limit in the absence of lensing. Assuming that galaxies are intrinsically randomly distributed, the probability of having  $N$  galaxies within  $\mathcal{U}$  is a Poisson distribution  $P_N(\langle N \rangle)$  with

$$\langle N \rangle = n_0 \int_{\mathcal{U}} d^2\theta \left| \mu(\vec{\theta}) \right|^{\beta-1}. \quad (27)$$

Consequently, the likelihood function could be augmented by a factor

$$\mathcal{L}_\mu = P_N(\langle N \rangle) \prod_{k=1}^N \left| \mu(\vec{\theta}_k) \right|^{\beta-1}. \quad (28)$$

If galaxy clustering is important, the likelihood  $\mathcal{L}_\mu$  cannot be written as a simple product over individual galaxies, but the joint probability distributions must be taken into account. The contribution of clustering effects to the likelihood function is somewhat uncertain, because an approximate expression has to be used due to lack of knowledge on the  $N$ -point correlation functions (see Broadhurst et al. 1995 for further discussion).

Perhaps the most promising generalization of our method is the inclusion of strong lensing constraints. Since giant arcs and multiple images of background galaxies provide (nearly) exact constraints on the lens mass distribution, it is highly desirable to include them into a mass reconstruction. The obvious way to do this would be to augment the function  $E$  by a term which measures the degree to which multiple images of the same source are mapped back to the same position in the source plane. In addition, the surface brightness profile of multiple images of extended sources can be incorporated, e.g. in a similar manner as the spatially resolved multiple arc in the cluster Cl0024+16 (Colley et al. 1996).

In some of the observed clusters, the lensing effects of individual galaxies are visible, in particular through deformations of giant arcs. Some of the most prominent examples are the triple arc in 0024+16 (Kassiola et al. 1992), the multiple arc systems in A 2218 (Kneib et al. 1996), and the distortion of the curvature in the arc of the galaxy cB58 in MS1512+36 (Seitz et al. 1998). But even weaker lensing effects of individual (cluster) galaxies can be detected using a combination of cluster mass reconstruction and galaxy-galaxy lensing techniques. By adding two free parameters to the lens model, such as the mass-to-light ratio of cluster galaxies and their characteristic spatial extent, the size of halos of cluster galaxies can be investigated (Natarayan et al. 1997; Geiger & Schneider 1998).

## Acknowledgements

This work was supported by the ‘‘Sonderforschungsbereich 375-95’’ f ur Astro-Teilchenphysik der Deutschen Forschungsgemeinschaft.

## A Notes on the implementation

We outline here how the function  $E$  – see (13) and (16) – can be calculated from the deflection potential  $\{\psi\}$  at the grid points. We first note that  $E$  can be easily calculated in terms of the shear  $\gamma$  and the surface mass density  $\kappa$  at the position of the galaxies  $\vec{\theta}_k$ , and in terms of  $\kappa$  at the grid points, which enters into the regularization term  $\mathcal{R}$ .

Let  $\psi_\alpha$  label the deflection potential at the  $N_{\text{dim}}$  grid points where  $\psi$  is varied. If no magnification information is used,  $N_{\text{dim}} = (N_x + 2)(N_y + 2) - 8$ , and  $N_{\text{dim}} = (N_x + 2)(N_y + 2) - 7$  otherwise. The components of  $\gamma$  and  $\kappa$  at the  $N_x N_y$  grid points are obtained by second-order finite differencing, according to (1) and (2). For calculating  $\gamma_2$  at the grid corners, we used the finite-difference formula (25.3.27) from Abramowitz & Stegun (1984) so that  $\psi$  at the corner points of the extended grid does not enter  $E$ . This can be important because the corner points do not enter the entropy term, so that they are not regularized. If no galaxy happens to lie in the corner grid cells, these points would be unconstrained. Finite differencing being a linear operation, we can write

$$\kappa_\mu = D_{\mu\alpha}\psi_\alpha + d_\mu, \quad 1 \leq \mu \leq N_x N_y. \quad (29)$$

Summation over  $\alpha$ ,  $1 \leq \alpha \leq N_{\text{dim}}$ , is implied, and the array  $d_\mu$  accounts for the contribution to  $\kappa_\mu$  from the grid points where  $\psi$  is held constant. For each galaxy position  $\vec{\theta}_k$ , the values of  $\kappa$  and  $\gamma$  are obtained from bilinear interpolation from the closest grid points. Since interpolation is again a linear operation, we can write

$$\begin{aligned} \gamma_1(\vec{\theta}_k) &= A_{k\alpha}\psi_\alpha + a_k, \\ \gamma_2(\vec{\theta}_k) &= B_{k\alpha}\psi_\alpha + b_k, \\ \kappa(\vec{\theta}_k) &= C_{k\alpha}\psi_\alpha + c_k, \end{aligned} \quad (30)$$

for  $1 \leq k \leq N_g$ . The arrays  $a$ ,  $b$ , and  $c$  again arise from the contributions of the grid points where  $\psi$  is held fixed. If magnification information is used,  $\psi$  is kept fixed at three grid points, where  $\psi = 0$  can be chosen without loss of generality; then,  $a_k = b_k = c_k = 0 = d_\mu$ . If magnification information is neglected, at least one of the four constant values of  $\psi$  has to differ from zero, and  $a$ ,  $b$ ,  $c$ , and  $d$  are not identically zero, although most of their elements vanish. The same holds for the elements of the matrices  $A$ ,  $B$ ,  $C$ , and  $D$ . Whereas the dimension of these matrices is large, only about  $12N_g$  elements are different from zero. Thus, we store these matrices using the row-indexed sparse storage mode, as described in Press et al. (1992, Sect. 2.7). Note that these matrices and ‘vectors’ have to be calculated only once, since they depend only on the number of grid points and the location of the galaxies. The sparseness of the matrices is one of the advantages to work in terms of the deflection potential rather than the surface mass density.

For the calculation of  $\partial E / \partial \psi_\alpha$ , we note that for any function  $f_k$  at  $\vec{\theta}_k$ ,

$$\frac{\partial f_k}{\partial \psi_\alpha} = \frac{\partial f_k}{\gamma_1(\vec{\theta}_k)} A_{k\alpha} + \frac{\partial f_k}{\gamma_2(\vec{\theta}_k)} B_{k\alpha} + \frac{\partial f_k}{\kappa(\vec{\theta}_k)} C_{k\alpha}. \quad (31)$$

For the regularization term, we find

$$\begin{aligned} \frac{\partial \mathcal{R}}{\partial \psi_\alpha} &= - \left[ \sum_{\mu=1}^{N_x N_y} \kappa_\mu \right]^{-1} \\ &\times \sum_{\mu=1}^{N_x N_y} \ln \left( \frac{\hat{\kappa}_\mu}{b_\mu} \right) \left[ D_{\mu\alpha} - \hat{\kappa}_\mu \sum_{\nu=1}^{N_x N_y} D_{\nu\alpha} \right]. \end{aligned} \quad (32)$$

Using these relations, the function  $E$  and its derivative with respect to the  $\psi_\alpha$  are easily calculated.

An additional complication arises for a critical lens. As can be seen from the explicit form of the terms of  $E$ , the likelihood function attains singularities if a galaxy image happens to lie on

a critical curve where  $|\delta| = 1$  and  $\mu^{-1} = 0$ . This means that the minimization procedure cannot modify the model such that critical curves move over galaxy positions. Since the initial guess of  $\psi$  will certainly not be accurate enough that such crossings can be avoided, we have to modify the function  $E$  appropriately. The necessary modification of  $E$  can be achieved by replacing  $|\mu|$  by  $[\mu^{-2} + \epsilon^2]^{-1/2}$ , and  $\sigma_\chi$  by  $\sigma_\chi + \eta$ , where  $\epsilon$  and  $\eta$  are two small quantities. These replacements leave  $E$  finite if a galaxy image is placed on a critical curve. The minimization then proceeds by setting  $\epsilon$  and  $\eta$  to about 0.1 at the beginning of the minimization, and then slowly decreasing them in later iteration steps. This leads to convergence without additional problems. In addition, as was true for the direct inversions, by considering a broad redshift distribution of the background galaxies (Seitz & Schneider 1997), the singularities connected with critical curves are avoided (Geiger & Schneider 1998).

## References

- [1] Abramowitz, M., Stegun, I. 1984, "Handbook of Mathematical Functions", Harri Deutsch Verlag
- [2] Bartelmann, M. 1995, A&A, 303, 643
- [3] Bartelmann, M., Narayan, R. 1995, ApJ, 451, 60
- [4] Bartelmann, M., Narayan, R., Seitz, S., Schneider, P. 1996, ApJ, 464, L115 (BNSS)
- [5] Blandford, R.D., Saust, A.B., Brainerd, T.G., Villumsen, J.V. 1991, MNRAS 251, 600
- [6] Bridle, S.L., Hobson, M.P., Lasenby, A.N., Saunders, R., 1998, astro-ph/9802159
- [7] Broadhurst, T.J., Taylor, A.N. Peacock, J.A. 1995, ApJ, 438, 49
- [8] Colley, W.N., Tyson, J.A., Turner, E.L. 1996, ApJ 461, L83
- [9] Fort, B., Mellier, Y., Dantel-Fort, M. 1997, A&A, 321, 353
- [10] Geiger, B., Schneider, P. 1998, in preparation
- [11] Gorenstein, M.V., Falco, E.E., Shapiro, I.I. 1988, ApJ, 327, 693
- [12] Kaiser, N., Squires, G. 1993, ApJ, 404, 441
- [13] Kaiser, N., Squires, G., Fahlmann, G.G., Woods, D., Broadhurst, T. 1994, astro-ph/9411029
- [14] Kaiser, N. 1995, ApJ, 493, L1
- [15] Kaiser, N., Squires, G., Broadhurst, T. 1995, ApJ, 449, 460
- [16] Kassiola, A., Kovner, I., Fort, B. 1992, APJ, 400, 41
- [17] Kneib, J.-P., Ellis, R.S., Smail, I., Couch, W.J., Sharples, R.M. 1996, ApJ 471, 643
- [18] Kolatt, T.S., Bartelmann, M. 1998, MNRAS, in press
- [19] Lombardi, M., Bertin, G. 1998, astro-ph/9801244
- [20] Lucy, L. 1994, A&A 289, 983
- [21] Narayan, R., Nityananda, R. 1986, ARA&A 24, 127
- [22] Natarayan, P., Kneib, J.-P., Smail, I., Ellis, R.S. 1997, astro-ph/9706129
- [23] Press, W.H., Teukolsky, S.A., Vetterling, W.T., Flannery, B.P. 1992, Numerical Recipes. Cambridge (Cambridge University Press)

- [24] Schneider, P. 1995, *A&A*, 302, 639
- [25] Schneider, P., Bartelmann, M. 1997, *MNRAS* 286, 673
- [26] Schneider, P., Seitz, C. 1995, *A&A*, 294, 411
- [27] Seitz, C., Schneider, P. 1995, *A&A*, 297, 287
- [28] Seitz, C., Kneib, J.P., Schneider, P., Seitz, S. 1996 *A&A*, 314, 707
- [29] Seitz, C., Schneider, P. 1997, *A&A*, 318, 617
- [30] Seitz, S., Schneider, P. 1996, *A&A*, 305, 383
- [31] Seitz, S. 1997, “Untersuchungen zum schwachen Linseneffekt auf Quasare und Galaxien”.  
Ph.D. Dissertation (in German), Ludwig-Maximilians-Universität München.
- [32] Seitz, S., Saglia, R.P., Bender, R., Hopp, U., Belloni, P., Ziegler, B. 1998, *MNRAS*, in press
- [33] Seitz, S., Schneider, P. 1998, *A&A* submitted, astro-ph/9802051
- [34] Squires, G., Kaiser, N. 1996, *ApJ*, 473, 65 (SK)